ARTICLE

# Red Blood Cell (RBC)-like Ni@N–C composites for Efficient Electrochemical $CO_2$ Reduction and Zn-$CO_2$ Battery

Received 00th January 20xx,
Accepted 00th January 20xx

DOI: 10.1039/x0xx00000x

Liu Han[a], Cheng-wei Wang[a], Hai-ping Xu[a], Ming Yang[b,c], Bing Li[*a], Ming Liu[*a]

The development of highly active and selective electrocatalysts for the reduction of $CO_2$ into valuable products presents a promising avenue for addressing the energy crisis and mitigating the greenhouse effect. In this study, we introduce a ligand-assisted supermolecule-derived red blood cell (RBC)-like catalyst composed of nickel and nitrogen-doped carbon (Ni@NC) for electrocatalytic carbon dioxide reduction reaction ($eCO_2RR$) and Zn-$CO_2$ battery applications. Among the various samples prepared, Ni@NC-950 exhibited the highest activity and demonstrated a faradaic efficiency of CO ($FE_{CO}$) greater than 90% across a wide potential range from -0.6 to -1.0 V [vs reversible hydrogen electrode (RHE)], with a peak $FE_{CO}$ of 98% achieved at -0.8 V. This translated to a remarkable partial current density ($J_{CO}$) of 22.5 mA·cm$^{-2}$. When employed as the cathode catalyst in a Zn-$CO_2$ battery, the Ni@NC-950 catalyst delivered a peak power density of 2.36 mW·cm$^{-2}$ at a current density of 10.97 mA·cm$^{-2}$. Importantly, the battery exhibited robust long-term discharge capability, operating continuously and steadily at 5 mA·cm$^{-2}$ for 20 hours.

## Introduction

The overreliance of industrial manufacturers on traditional fossil energy has exacerbated a severe energy crisis, while the consumption of fossil energy leads to significant $CO_2$ emissions, further intensifying the greenhouse effect on the environment. In recent years, research on carbon capture, utilization, and storage (CCUS) technology has gained significant attention. Consequently, the exploration of sustainable new energy sources and the reduction of $CO_2$ emissions are fundamental approaches to address the aforementioned challenges.[1-8] Presently, electrocatalytic $CO_2$ reduction reaction ($eCO_2RR$), driven by clean electric energy, presents a remarkable advantage in the utilization of $CO_2$ resources. This process not only helps mitigate the increasing levels of atmospheric $CO_2$ but also enables the production of high-value-added chemicals or fuels, thereby facilitating a sustainable global carbon cycle.[9-11] However, the overall performance of $eCO_2RR$ still faces challenges in terms of activity, selectivity, and durability due to the thermodynamic stability and chemical inertness of $CO_2$ molecules, as well as the competing hydrogen evolution reaction (HER).[12-14] Therefore, there is an urgent need to develop cost-effective and abundant electrocatalysts that exhibit highly efficient catalytic activity and selectivity for $eCO_2RR$.

The two-electron transfer product, carbon monoxide (CO), is widely recognized as one of the most abundant and accessible products in the electrocatalytic $CO_2$ reduction reaction ($eCO_2RR$) process.[15, 16] Its high economic value and energy density make it highly promising for various applications, such as the Fischer-Tropsch reaction and fuel cells.[17, 18] Among the reported electrocatalysts, metal-nitrogen-doped carbon (M@NC) materials have emerged as promising candidates for $CO_2$ conversion to CO due to their cost-effectiveness and remarkable performance, surpassing even noble-metal-based Au and Ag electrocatalysts.[19-22] Within the realm of M@NC electrocatalysts, nickel-nitrogen-doped carbon (Ni@NC) materials have been identified as optimal in terms of CO selectivity and current density, primarily attributed to the reduced free energy required for the conversion of $CO_2$ to adsorbed *COOH species.[23, 24]

Numerous strategies have been proposed for the synthesis of Ni@NC catalysts in $eCO_2RR$. Typically, the synthesis involves the co-pyrolysis of transition metal salts and nitrogen-rich organic precursors.[25, 26] However, catalysts derived from such co-pyrolysis processes often suffer from irregular morphologies, low specific surface areas, and ineffective pore structures, resulting in diminished CO selectivity and limited partial current density.[27] To address these challenges, Ni@NC catalysts derived from metal-organic frameworks (MOFs) have been explored, effectively circumventing the aforementioned shortcomings. Nonetheless, the long reaction time and low yield of MOFs render them unsuitable for large-scale production and application.[28, 29] As a result, the utilization of magnesium oxide (MgO) or other inert porous materials as templates for the preparation of high-activity electrocatalysts has been investigated. However, the harsh conditions required for

[a] School of Chemistry and Chemical Engineering, Harbin Institute of Technology, Heilongjiang Province, 150000, China. E-mail addresses: BL: bing.li2020@hit.edu.cn; ML: liuming0117@hit.edu.cn;
[b] Department of Applied Physics, The Hong Kong Polytechnic University, Hung Hom, Hong Kong SAR, China.
[c] Research Centre on Data Sciences & Artificial Intelligence, The Hong Kong Polytechnic University, Hung Hom, Hong Kong SAR, China.

template removal have hindered further development in this area.[30-32] Therefore, there is a pressing need to explore a facile synthetic route that enables the preparation of Ni@NC catalysts with unique structures and accessible pores, thereby enhancing the performance of $eCO_2RR$.

Recently, the utilization of $C_3N_4$ as a self-sacrificial template for the preparation of M@NC catalysts has gained significant attention.[33, 34] During the pyrolysis process, $C_3N_4$ undergoes decomposition, resulting in the formation of gas molecules and the subsequent creation of hollow or porous structures within the catalyst. Simultaneously, the decomposed gas molecules permeate the nitrogen-doped carbon matrix that forms in situ, generating diverse types of pores. This phenomenon contributes to an increase in the specific surface area of the catalyst, facilitating the efficient transfer of protons and electrons and thereby enhancing the kinetics of the catalytic reaction. Notably, $C_3N_4$ derived from the molecular cooperative assembly method using melamine and cyanuric acid supramolecular precursors exhibits an enhanced surface area and an abundance of pores. This facile approach enables the facile synthesis of $C_3N_4$ with desirable characteristics, further augmenting its potential for various applications.[35, 36]

In this study, we present a facile ligand-assisted molecular cooperative assembly strategy combined with a subsequent annealing treatment method for the synthesis of nickel and nitrogen-doped carbon (Ni@NC) composites with a morphology resembling that of red blood cells (RBCs). These composites exhibit exceptional electrocatalytic performance in the electrochemical reduction of $CO_2$ ($eCO_2RR$). Specifically, the Ni@NC-950 sample demonstrates a remarkable faradaic efficiency for CO ($FE_{CO}$) exceeding 90% over a wide potential range of -0.6 to -1.0 V vs RHE, with a peak value of 98% observed at -0.8 V vs RHE. Furthermore, when employed as a cathode catalyst in a flow cell, the Ni@NC-950 sample exhibits a high CO selectivity and achieves an industrially relevant current density of 204 $mA{\cdot}cm^{-2}$ at -1 V. Additionally, we successfully assemble a Zn-$CO_2$ battery using Ni@NC-950 as the cathode catalyst, which demonstrates a peak power density of 2.36 $mW{\cdot}cm^{-2}$. The battery maintains stable performance for over 20 hours at a discharge current density of 5 mA $cm^{-2}$, with the discharge voltage remaining nearly constant throughout the operation.

## Results and Discussion

### Fabrication and Structural Characterizations of Ni@NC-T

In this study, a ligand-assisted supermolecule was utilized as the precursor for the synthesis of red blood cell (RBC)-like nickel and nitrogen-doped carbon (Ni@NC-T; T refers to the pyrolysis temperature, T = 800, 900, 950, and 1000). A schematic representation of the molecular cooperative assembly strategy is depicted in Figure 1a. Initially, metal-ligand chelates were prepared by the reaction of $Ni^{2+}$ with Phenanthroline (Ph). Subsequently, a mixture of the prepared chelates and cyanuric acid was combined with a melamine solution, leading to the self-assembly of the chelate-supermolecule complex (Ni-PMCA) through hydrogen bonding. Finally, the RBC-like Ni@NC-T was obtained by subjecting the precursor to pyrolysis at the desired temperature under an $N_2$ atmosphere. During the thermal treatment process, the MCA supermolecule underwent decomposition, acting as a template for the formation of the RBC-like structure while releasing gases containing N, C, and O. Simultaneously, the metal-ligand chelates transformed into nickel and nitrogen-doped carbon (Ni@NC).

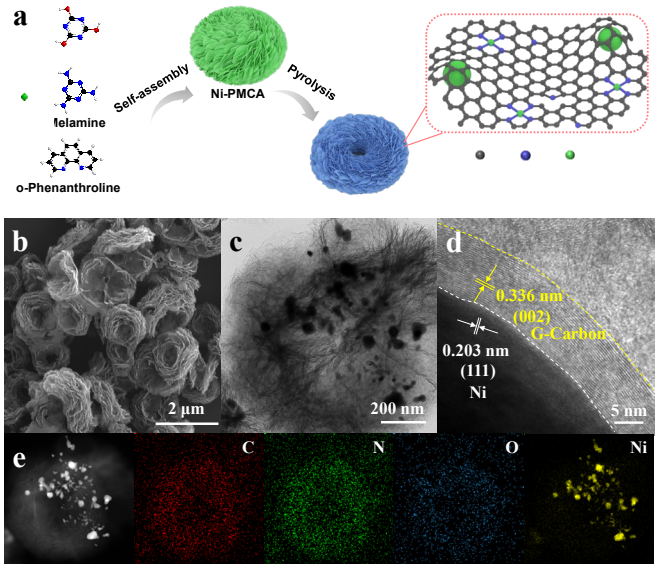


Fig. 1 Catalysts preparation process and morphology characterizations. (a) A schematic illustration of the preparation process for Ni@NC-T. (b-d) SEM, TEM and HRTEM images of Ni@NC-950. (e) Corresponding EDS mapping of Ni@NC-950 from (c), showing the dispersion of C (red), N (green), O (blue), and Ni (yellow).

Scanning electron microscopy (SEM, Fig. S1a) revealed the uniform size (2 μm) and typical spherical structure with a rough surface of the chelate-supermolecule complex. In Fig. 1b, the Ni@NC-950 sample exhibited a significant reduction in overall dimensions after thermal treatment, presenting a morphology resembling stacked nanosheets, akin to red blood cells. This morphology potentially facilitates enhanced electron transport and gas diffusion. Transmission electron microscopy (TEM) images (Fig. 1c) demonstrated that the RBC-like Ni@NC-950 sample possessed unique hollow structures assembled from nanosheets. Additionally, randomly distributed Ni nanoparticles (NPs) were observed within the hierarchical carbon matrix. High-resolution TEM (HRTEM) images (Fig. 1d) displayed the characteristic structure of carbon-encapsulated Ni NPs. The observed lattice fringes with the spacing of 0.203 nm in the core region and 0.336 nm in the shell region corresponded to the (111) plane of Ni and (002) plane of graphitic carbon, respectively. Energy-dispersive X-ray spectroscopy (EDS) mapping images (Fig. 1e) revealed the homogeneous distribution of C, N, and O elements, while the Ni particles were randomly dispersed on the carbon matrix.

To investigate the impact of pyrolysis temperature on the structure of the catalyst, a series of Ni@NC-T samples were prepared using similar methods but with different pyrolysis temperatures. All samples exhibited RBC-like hierarchical

hollow structures assembled from stacked nanosheets (Fig. S2-7, ESI†). X-ray diffraction (XRD) spectra revealed a broad peak between 20 to 25° in all Ni@NC-T samples, corresponding to the (002) lattice plane of graphitic carbon. Additionally, three peaks at 44.5°, 51.9°, and 76.4° were observed in the Ni@NC-900, Ni@NC-950, and Ni@NC-1000 samples, respectively, corresponding to the (111), (200), and (220) planes of metallic Ni (JCPDF No. 04–0850) (Fig. 2a). Moreover, the intensity of the Ni diffraction peak gradually increased with higher pyrolysis temperatures. This phenomenon can be attributed to

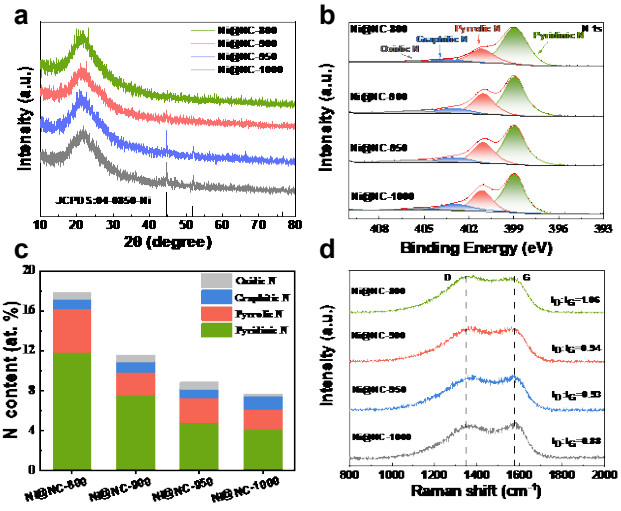


Fig. 2 The structure characterizations of catalysts. (a) XRD pattern, (b) N 1s XPS spectra, (c) corresponding contents of N species, and (d) Raman spectra of four Ni@NC-T samples.

the Oswald phenomenon, where smaller particles aggregate and fuse into larger ones at higher temperatures, reducing the surface free energy.[37, 38]

The elemental composition and chemical states of the four samples were investigated using X-ray photoelectron spectroscopy (XPS). The high-resolution C 1s spectrum exhibited three deconvoluted peaks at 284.8 eV, 285.8 eV, and 288.4 eV, corresponding to C-C, C-N, and O-C-O, respectively (Fig. S8). The high-resolution Ni 2p spectrum displayed peaks at 853.3 eV and 855.3 eV, which can be assigned to metallic $Ni^0$ and $Ni^{2+}$, respectively (Fig. S9, ESI†). Notably, the peak position gradually shifted from $Ni^{2+}$ to $Ni^0$ with increasing pyrolysis temperature, indicating the transformation of individual Ni species on the surface into Ni nanoparticles (NPs) at higher temperatures. The N 1s binding energy in the samples was divided into pyridinic-N (~398.6 eV), pyrrolic-N (~400.6 eV), graphitic-N (~401.9 eV), and oxidized-N (~403.9 eV).[39] The content of each nitrogen species was calculated and is presented in Fig. 2b and c. Pyridinic-N and pyrrolic-N were identified as the main N-species in all four samples. The total nitrogen content decreased with increasing pyrolysis temperature. Specifically, the pyridinic-N content declined from 11.8% in Ni@NC-800 to 7.51% in Ni@NC-900, 4.82% in Ni@NC-950, and 4.13% in Ni@NC-1000, respectively. Prior research has indicated that pyridinic-N favors hydrogen evolution reaction (HER) for $H_2$ production,[40, 41] Therefore, the decrease in pyridinic N content at higher temperatures could be beneficial in suppressing the competitive HER in $eCO_2RR$.

The Raman spectrum of all samples exhibited two distinct peaks at approximately 1350 and 1590 $cm^{-1}$, corresponding to disordered sp3 carbon (D band) and graphitic $sp^2$ carbon (G band), respectively (Fig. 2d). The gradual decrease in the ratio of the D band to the G band's relative intensity with increasing pyrolysis temperature indicated an enhanced extent of graphitization and reduced nitrogen defect density, consistent with the high-resolution N 1s spectrum.

Nitrogen adsorption-desorption isotherms displayed an IV-type isotherm for all samples, indicating the presence of abundant micro- and mesoporous structures (Fig. S10, ESI†). The pore size distribution analysis revealed that both microporous and mesoporous regions dominated the pore structure of the four samples, confirming the typical hierarchical porous architecture. The Brunauer-Emmett-Teller (BET) specific surface area of the four samples was approximately 450 $m^2 \cdot g^{-1}$, facilitating mass transport and exposing more active sites.

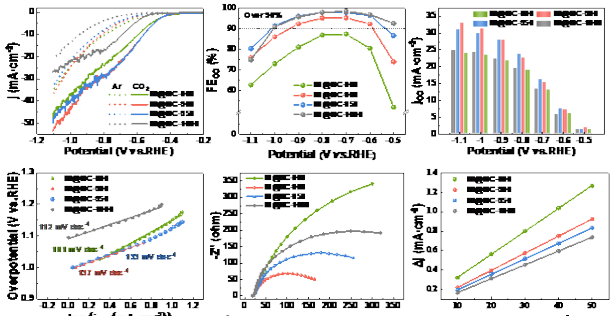


Fig. 3 Electrocatalytic performance: a) LSV curves in Ar/$CO_2$-saturated 0.5 M $KHCO_3$ electrolyte at a scan rate of 20 $mV \cdot s^{-1}$ for the different catalysts. b) $FE_{CO}$ and c) $J_{CO}$ of Ni@N-T in the H-type cell. d) Tafel plots, e) Nyquist plots, and f) dependence of charging current density differences (Δj) versus scan rates of Ni@N-T samples. g) The current density and Faraday efficiency for the Ni@NC-950 sample before and after KSCN were added. h) Durability test at -0.8 V of the Ni@NC-950 sample in H-cell.

**Electrocatalytic Properties**

The electrocatalytic $CO_2$ reduction reaction ($eCO_2RR$) performance of the four samples was evaluated in a gas-tight H-type cell using an Ag/AgCl electrode as the reference electrode and a commercial graphite rod as the counter electrode (Fig. S11, ESI†). It is important to note that all potentials reported in this study are referenced to the reversible hydrogen electrode (RHE) without iR (i, current; R, resistance) correction. Comparing the linear sweep voltammetry (LSV) results in an Ar-saturated 0.5 M $KHCO_3$ solution with those in a $CO_2$ atmosphere, all four samples exhibited higher current densities in the $CO_2$ atmosphere, indicating their $eCO_2RR$ activity (Fig. 3a). Chronoamperometric electrolysis was conducted to further investigate the activity and selectivity of the synthesized catalysts. Gas chromatography (GC) spectra revealed only the presence of $H_2$ and CO as the reaction products (Fig. S12, ESI†), with no liquid products detected in the $^1H$ nuclear magnetic resonance (NMR) analysis (Fig. S13, ESI†). Fig. 3b presents the CO Faradaic efficiency ($FE_{CO}$) results obtained within the potential

range of -0.5 to -1.1 V for the four samples. One can see that Ni@NC-950 and Ni@NC-1000 illustrated higher $FE_{CO}$ values compared to Ni@NC-900, particularly between -0.6 to -1.0 V, while Ni@NC-800 exhibited the lowest selectivity for CO production among the samples. This trend suggests that increasing the pyrolysis temperature helps the Ni@NC-T to achieve better CO selectivity, i.e. reducing the competitive HER in $eCO_2RR$ (Fig. S14, ESI†). This observation aligns with the decrease in pyridinic N content at elevated temperatures, as depicted in Fig. 2c, which is consistent with findings from previous studies.[40, 41] Notably, the $FE_{CO}$ of the Ni@NC-950 sample exceeded 90% over a wide potential range (-0.6 to -1.0 V versus RHE) and reached 97.8% at -0.8 V, with a corresponding partial current density of CO ($j_{CO}$) of up to 23.8 $mA{\cdot}cm^{-2}$. To the best of our knowledge, our prepared catalysts displayed excellent $FE_{CO}$ compared to previous studies on Ni-based electrocatalysts (Fig. S15, S16, and Table S1, ESI†). It is worth noting that the trend in the $j_{CO}$ of these samples did not follow that of $FE_{CO}$. The Ni@NC-950 sample exhibited the highest $j_{CO}$ from -0.6 to -0.8 V, while the Ni@NC-900 sample surpassed it at applied potentials larger than -0.8 V due to enhanced HER at high potentials, leading to an increase in the total current. However, the Ni@NC-800 sample consistently exhibited the lowest $j_{CO}$ (Fig. 3c).

The electrochemical behaviors of the prepared samples were further analyzed to understand the relationship between pyrolysis temperature and electrocatalytic performance. Tafel plots were employed to reveal the reaction kinetics of the four samples (Fig. 3d). The Tafel slopes of Ni@NC-800 (181 $mV{\cdot}s^{-1}$), Ni@NC-900 (137 $mV{\cdot}s^{-1}$), Ni@NC-950 (133 $mV{\cdot}s^{-1}$), and Ni@NC-1000 (112 $mV{\cdot}s^{-1}$) were all close to 118 $mV{\cdot}s^{-1}$, indicating that the rate-determining step of the $eCO_2RR$ is the first electron transfer process to form $CO_2^{\bullet-}$ radical anions. The smaller Tafel slope values suggest favorable kinetics for $eCO_2RR$ in Ni@NC-950 and Ni@NC-1000. Additionally, electrochemical impedance spectroscopy (EIS) revealed that the Ni@NC-900 and Ni@NC-950 samples exhibited significantly lower charge-transfer resistance compared to Ni@NC-800 and Ni@NC-1000 (Fig. 3e), thereby facilitating the electrochemical reduction of $CO_2$. It is generally believed that a larger electrochemical active surface area (ECSA) corresponds to a higher number of active sites on the catalyst. However, this principle does not universally apply, particularly in strongly hydrophobic environments.[42-44] In our case, the ECSA showed a positive correlation with the hydrophobic performance of the catalysts. Catalysts with strong hydrophobic properties impede the penetration of the electrolyte into the catalyst's interior, allowing only external contact between the catalyst and the electrolyte. Consequently, we initially assessed the hydrophobicity of the four prepared catalysts through contact angle experiments (Fig. S17, ESI†). The results indicated a correlation between catalyst hydrophobicity and the pyrolysis temperature, with the Ni@NC-1000 and Ni@NC-800 samples exhibiting the strongest and weakest hydrophobicity, respectively. Subsequently, the ECSA was determined by measuring the double-layer capacitance (CdI) in a non-faraday region (Fig. S18, ESI†). As depicted in Fig. 3f, the Ni@NC-800 sample exhibited the highest Cdl value of 11.9 $mF{\cdot}cm^{-2}$, surpassing the Ni@NC-900 (8.8 $mF{\cdot}cm^{-2}$), Ni@NC-950 (8.0 $mF{\cdot}cm^{-2}$), and Ni@NC-1000 (7.2 $mF{\cdot}cm^{-2}$). These ECSA results align with the hydrophobicity of the catalysts, suggesting the formation of a more extensive tri-phase interface in the Ni@NC-950 and Ni@NC-1000 samples. The tri-phase interface plays a crucial role in promoting the electrochemical $CO_2RR$ while inhibiting the HER, thereby enhancing CO selectivity. While Ni@NC-800 exhibits the highest Cdl value (indicating the largest ECSA), its ESCA-normalized JCO is the smallest among the four samples (Fig. S19, ESI†). This verifies the beneficial effect of higher pyrolysis temperatures in enhancing CO selectivity for Ni@NC-T. It also suggests that a higher ESCA does not always represent more electrochemical active sites and the catalytic activity of a catalyst is closely linked to the surface composition and chemical environment, including N-doping in our case. Furthermore, the pyrolysis temperature can influence the Ni loading in Ni@NC-T, in turn impacting its catalytic behavior to a certain extent. The turnover frequency (TOF) of the Ni@NC-T was calculated and summarized in Fig. S20. The TOF of all Ni@NC-T samples gradually increases with the increasing overpotential. However, comprehensively understanding the role of Ni species in JCO is challenging due to the diverse and complex nature of Ni species in our samples, which may include particles of varying sizes, clusters, possibly dispersed Ni single or double atoms, and varying thicknesses of carbon coatings on the Ni particles. Further research is required in this area, and it will be one of the focuses of our future investigations.

Based on the aforementioned analyses, the outstanding activity of the Ni@NC-950 sample in terms of $FE_{CO}$ and $j_{CO}$ can be primarily attributed to the synergistic effects of fast reaction kinetics, low electron transfer resistance, and excellent hydrophobicity. Furthermore, a poison experiment was conducted to investigate the contribution of Ni-$N_X$ active sites to $eCO_2RR$ (Fig. 3g). The Ni@NC-950 sample exhibited nearly unchanged current density and $FE_{CO}$ after the addition of KSCN, indicating the negligible role of Ni-$N_X$ active sites. To assess the $eCO_2RR$ stability of the Ni@NC-950 sample, a long-term $CO_2$ reduction test was performed at -0.8 V. As shown in Fig. 3h, the current density and CO selectivity of the Ni@NC-950 sample remained stable even after 12 hours of continuous operation, demonstrating its excellent catalytic durability. Moreover, the XRD pattern confirmed that the crystalline structure of the Ni@NC-950 sample remained unaltered after the stability test (Fig. S20, ESI†), while SEM images revealed that the morphology of the Ni@NC-950 sample retained its hierarchical structure (Fig. S21, ESI†).

**Flow cell**

As we know, conventional H-type cells often suffer from inadequate mass transfer, resulting in limited current density, which poses challenges for the industrial-scale application of electrochemical $eCO_2RR$. To address this issue, the implementation of a flow cell with a three-phase boundary comprising the catalyst, electrolyte, and $CO_2$ gas has proven effective in overcoming the limitations associated with the low

 

solubility of $CO_2$ molecules in solution (Fig. 4a and S22, ESI†).[10, 45] As anticipated, the current density of the Ni@NC-950 sample in the flow cell exhibited significant enhancement compared to that observed in the H-type cell, accompanied by

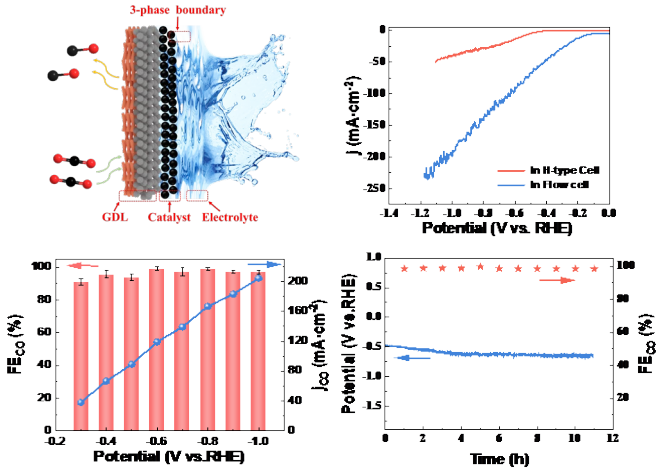


Fig. 4 (a) Schematic diagram of gas diffusion electrode. (b) LSV curves of the Ni@NC-950 sample in the H-type cell and flow cell. (c) $FE_{CO}$ and $J_{CO}$ with different applied potentials of the Ni@N-950 sample in the flow cell. (d) Long-term stability tests of the Ni@N-950 sample at -100 mA·cm$^{-2}$ in the flow cell.

a reduction of 0.3 V in the onset potential (Fig. 4b). Additionally, chronoamperometry electrolysis conducted in the flow cell demonstrated that the Ni@NC-950 sample achieved $FE_{CO}$ values exceeding 90% over a wide potential range from -0.3 to -1.0 V. Furthermore, the $j_{CO}$ rapidly increased from 38 mA·cm$^{-2}$ at -0.3 V to 204 mA·cm$^{-2}$ at -1 V (Fig. 4c).

Most notably, there was no noticeable drop in the applied potential, and the CO selectivity consistently remained at 98% during 10 hours of continuous electrolysis at -100 mA·cm$^{-2}$, showcasing the tremendous potential of our prepared catalyst for $eCO_2RR$ (Fig. 4d). It should be noted that the challenges of flooding in gas diffusion electrodes under high current density and the deposition of carbonates on the electrode during prolonged electrolysis hinder further advancements, a phenomenon observed in previous studies as well.

**Zn-$CO_2$ battery**

To further evaluate the exceptional $eCO_2RR$ performance of the Ni@NC-950 sample, a custom-made Zn-$CO_2$ battery was employed (Fig. 5a).

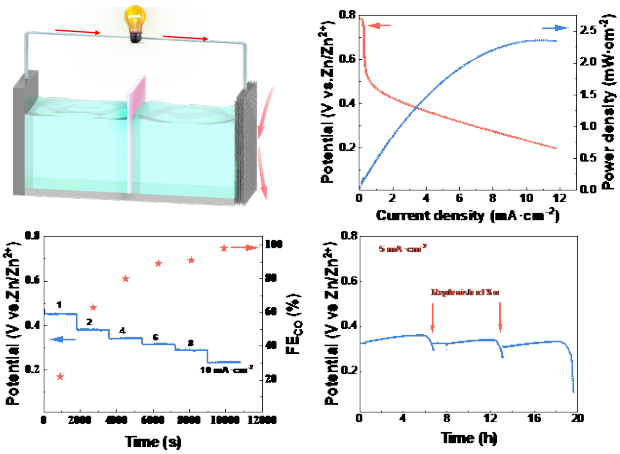


Fig. 5 (a) Schematic configuration of a Zn-$CO_2$ battery (b) Discharge polarization curve and corresponding power density curve of the Zn-$CO_2$ battery utilizing Ni@NC-950 catalyst. (c) galvanostatic discharge curves at different current densities and corresponding $FE_{CO}$. (d) Voltage profile of the Zn–$CO_2$ battery with two mechanical discharge cycles.

The cathode consisted of a Ni@NC-950 electrocatalyst-coated gas diffusion electrode (GDE), while a polished Zn plate served as the anode. A bipolar membrane was utilized to separate the catholyte (1 M $KHCO_3$) and anolyte (6 M KOH), ensuring pH stability on each side and preventing cross-contamination. Throughout the discharge process, $CO_2$ gas was continuously supplied to the gas chamber at a flow rate of 20 standard cubic centimeters per minute (sccm). The discharge polarization curve revealed that our assembled Zn-$CO_2$ battery exhibited an open circuit voltage of 0.785 V, in agreement with the theoretical value range of 0.7 V to 0.83 V (Fig. 5b).[46, 47] Impressively, the Ni@NC-950 cathode achieved a peak power density of 2.36 mW·cm$^{-2}$ at a current density of 10.97 mA·cm$^{-2}$, on par with the best performance of recently reported Zn-$CO_2$ batteries (refer to Table S2, ESI† for detailed comparisons). Nevertheless, the discharge current density in the Zn-$CO_2$ battery is significantly lower compared to the current density of eCO2RR in the flow cell, similar to existing literature. The LSV curves of anodic Zn oxidation of the Zn plate in 6 M KOH solution confirm the negligible effect of the Zn anode in current density (Fig. S24, ESI†). The lower current density in the Zn-$CO_2$ battery can be attributed, at least partially, to two key factors: 1) the large distance between the anode and cathode (2 cm in the Zn-$CO_2$ battery versus 0.5 cm of the gap between working and counter electrodes) inevitably increases the internal resistance and consequently reducing the actual discharge current of the battery, and 2) The composition, concentration and flow rate of the electrolyte. Therefore, to further improve the performance of a Zn-$CO_2$ battery, optimizing the battery configuration is important. This can be achieved by minimizing the distance between the anode and cathode and updating electrolyte composition and peristaltic electrolyte. Moreover, the battery with Ni@NC-950 catalyst demonstrated stable discharge capabilities at various discharge current densities, with a maximum $FE_{CO}$ reaching 98% at 10 mA·cm$^{-2}$ (Fig. 5c). Fig. 5d, the battery maintained its discharge at a current density of 5 mA·cm$^{-2}$ for over 20 hours across two mechanical charge cycles, involving the replacement of the zinc foil.

## Conclusions

In this study, we present the synthesis of red blood cell (RBC)-like catalysts based on nickel and nitrogen-doped carbon (Ni@NC-T) for electrocatalytic carbon dioxide reduction reaction ($eCO_2RR$). The catalysts were prepared using a ligand-assisted supramolecular self-assembly strategy, followed by pyrolysis at various temperatures. Notably, the Ni@NC-T catalysts exhibited remarkable electrocatalytic activity for $eCO_2RR$. Specifically, the Ni@NC-950 catalyst demonstrated exceptional CO selectivity and activity, achieving a faradaic efficiency of CO ($FE_{CO}$) of 98% and a partial current density ($j_{CO}$) of 22.5 mA·cm$^{-2}$ at -0.8 V in the H-type cell configuration. Moreover, the Ni@NC-950 catalyst maintained a high $FE_{CO}$ (>90%) over a wide potential range from -0.3 to -1.1 V and exhibited an impressive industrial current density of 204 mA·cm$^{-2}$ at -1 V. Furthermore, the catalyst demonstrated

robust stability during long-period $eCO_2RR$ experiments conducted in a flow cell setup. Additionally, the assembled Zn-$CO_2$ battery, utilizing the Ni@NC-950 catalyst as the cathode, exhibited a peak power density of 2.36 $mW \cdot cm^{-2}$ at a current density of 10.97 $mA \cdot cm^{-2}$. The battery not only surpassed the $CO_2$ reduction ability of previous systems but also demonstrated excellent current stability. Furthermore, the homemade Zn-$CO_2$ battery exhibited a discharge performance of over 20 hours at a discharge current density of 5 $mA \cdot cm^{-2}$, maintaining an almost constant discharge voltage through mechanical charging.

## Author Contributions

Liu Han: writing-original draft, data curation, methodology. Chengwei Wang: data analysis. Haiping Xu: data analysis. Ming Yang: image and software. Bing Li: supervision. Ming Liu: funding-acquisition, writing-review & editing, project administration.

## Conflicts of interest

The authors declare that they have no competing financial interests or personal relationships that could have appeared to influence the work reported in this paper.

## Acknowledgments

This work was supported by the Fundamental Research Funds for the Central Universities (China) and the Fundamental Science Research of Harbin Institute of Technology (No. AUGA2160100119; AUGA9803100120; AUGA5710001120；AUIQ1640100123). M.Y. acknowledges the funding support from The Hong Kong Polytechnic University (project numbers: ZE2F, CE04, and ZE2X) and PolyU RCNN (project no.: CE0H).

## Notes and references

1. J. D. Shakun, P. U. Clark, F. He, S. A. Marcott, A. C. Mix, Z. Liu, B. Otto-Bliesner, A. Schmittner and E. Bard, *Nature*, 2012, **484**, 49-54.
2. N. Thonemann and M. Pizzol, *Energy & Environmental Science*, 2019, **12**, 2253-2263.
3. C. A. Trickett, A. Helal, B. A. Al-Maythalony, Z. H. Yamani, K. E. Cordova and O. M. Yaghi, *Nature Reviews Materials*, 2017, **2**, 17045.
4. K. S. Song, P. W. Fritz and A. Coskun, *Chemical Society Reviews*, 2022, **51**, 9831-9852.
5. S. M. Kim, P. M. Abdala, M. Broda, D. Hosseini, C. Copéret and C. Müller, *ACS Catalysis*, 2018, **8**, 2815-2823.
6. Y. Hu, R. Abazari, S. Sanati, M. Nadafan, C. L. Carpenter-Warren, A. M. Z. Slawin, Y. Zhou and A. M. Kirillov, *ACS Applied Materials & Interfaces*, 2023, **15**, 37300-37311.
7. J. He, X. Wang, S. Lan, H. Tao, X. Luo, Y. Zhou and M. Zhu, *Applied Catalysis B: Environmental*, 2022, **317**.
8. J. Chen, R. Abazari, K. A. Adegoke, N. W. Maxakato, O. S. Bello, M. Tahir, S. Tasleem, S. Sanati, A. M. Kirillov and Y. Zhou, *Coordination Chemistry Reviews*, 2022, **469**.
9. F. Li, Y. C. Li, Z. Wang, J. Li, D.-H. Nam, Y. Lum, M. Luo, X. Wang, A. Ozden, S.-F. Hung, B. Chen, Y. Wang, J. Wicks, Y. Xu, Y. Li, C. M. Gabardo, C.-T. Dinh, Y. Wang, T.-T. Zhuang, D. Sinton and E. H. Sargent, *Nature Catalysis*, 2019, **3**, 75-82.
10. J. Li, G. Chen, Y. Zhu, Z. Liang, A. Pei, C.-L. Wu, H. Wang, H. R. Lee, K. Liu, S. Chu and Y. Cui, *Nature Catalysis*, 2018, **1**, 592-600.
11. R. Francke, B. Schille and M. Roemelt, *Chemical Reviews*, 2018, **118**, 4631-4701.
12. Y. Y. Birdja, E. Pérez-Gallent, M. C. Figueiredo, A. J. Göttle, F. Calle-Vallejo and M. T. M. Koper, *Nature Energy*, 2019, **4**, 732-745.
13. Z. Sun, T. Ma, H. Tao, Q. Fan and B. Han, *Chem*, 2017, **3**, 560-587.
14. K. Elouarzaki, V. Kannan, V. Jose, H. S. Sabharwal and J. M. Lee, *Advanced Energy Materials*, 2019, **9**, 1900090.
15. J. Wang, Y.-C. Huang, Y. Wang, H. Deng, Y. Shi, D. Wei, M. Li, C.-L. Dong, H. Jin, S. S. Mao and S. Shen, *ACS Catalysis*, 2023, **13**, 2374-2385.
16. S. Jin, Z. Hao, K. Zhang, Z. Yan and J. Chen, *Angewandte Chemie International Edition*, 2021, **60**, 20627-20648.
17. I. A. W. Filot, R. A. van Santen and E. J. M. Hensen, *Angewandte Chemie International Edition*, 2014, **53**, 12746-12750.
18. Y. Yang, F. Y. Gao, X. L. Zhang, S. Qin, L. R. Zheng, Y. H. Wang, J. Liao, Q. Yang and M. R. Gao, *Angewandte Chemie International Edition*, 2022, **61**, e202208040
19. F. Pan, B. Li, E. Sarnello, Y. Fei, Y. Gang, X. Xiang, Z. Du, P. Zhang, G. Wang, H. T. Nguyen, T. Li, Y. H. Hu, H.-C. Zhou and Y. Li, *ACS Nano*, 2020, **14**, 5506-5516.
20. F. Pan, B. Li, E. Sarnello, Y. Fei, X. Feng, Y. Gang, X. Xiang, L. Fang, T. Li, Y. H. Hu, G. Wang and Y. Li, *ACS Catalysis*, 2020, **10**, 10803-10811.
21. Z. Zhang, J. Xiao, X. J. Chen, S. Yu, L. Yu, R. Si, Y. Wang, S. Wang, X. Meng, Y. Wang, Z. Q. Tian and D. Deng, *Angewandte Chemie International Edition*, 2018, **57**, 16339-16342.
22. Y. Wang, Y. Liu, W. Liu, J. Wu, Q. Li, Q. Feng, Z. Chen, X. Xiong, D. Wang and Y. Lei, *Energy & Environmental Science*, 2020, **13**, 4609-4624.
23. X.-M. Hu, H. H. Hval, E. T. Bjerglund, K. J. Dalgaard, M. R. Madsen, M.-M. Pohl, E. Welter, P. Lamagni, K. B. Buhl, M. Bremholm, M. Beller, S. U. Pedersen, T. Skrydstrup and K. Daasbjerg, *ACS Catalysis*, 2018, **8**, 6255-6264.
24. S. Liang, L. Huang, Y. Gao, Q. Wang and B. Liu, *Advanced Science*, 2021, **8**, 2102886.
25. Y. Zhang, X. Wang, S. Zheng, B. Yang, Z. Li, J. Lu, Q. Zhang, N. M. Adli, L. Lei, G. Wu and Y. Hou, *Advanced Functional Materials*, 2021, **31**, 2104377.
26. D. Xi, J. Li, J. Low, K. Mao, R. Long, J. Li, Z. Dai, T. Shao, Y. Zhong, Y. Li, Z. Li, X. J. Loh, L. Song, E. Ye and Y. Xiong, *Advanced Materials*, 2021, **34**, 2104090.
27. H. Guo, D.-H. Si, H.-J. Zhu, Q.-X. Li, Y.-B. Huang and R. Cao, *eScience*, 2022, **2**, 295-303.
28. Y. Zhang, L. Jiao, W. Yang, C. Xie and H. L. Jiang, *Angewandte Chemie International Edition*, 2021, **60**, 7607-7611.
29. W. Ren, X. Tan, W. Yang, C. Jia, S. Xu, K. Wang, S. C. Smith and C. Zhao, *Angewandte Chemie International Edition*, 2019, **58**, 6972-6976.
30. M. Huang, B. Deng, X. Zhao, Z. Zhang, F. Li, K. Li, Z. Cui, L.

 

Kong, J. Lu, F. Dong, L. Zhang and P. Chen, *ACS Nano*, 2022, **16**, 2110-2119.
31. B. Chen, B. Li, Z. Tian, W. Liu, W. Liu, W. Sun, K. Wang, L. Chen and J. Jiang, *Advanced Energy Materials*, 2021, **11**, 2102152.
32. Z. Zhu, Z. Li, J. Wang, R. Li, H. Chen, Y. Li, J. S. Chen, R. Wu and Z. Wei, *eScience*, 2022, **2**, 445-452.
33. F. X. Ma, Z. Q. Liu, G. Zhang, H. S. Fan, Y. Du, L. Zhen and C. Y. Xu, *Small*, 2023, **19**, 2207991.
34. Y. Lu, H. Wang, P. Yu, Y. Yuan, R. Shahbazian-Yassar, Y. Sheng, S. Wu, W. Tu, G. Liu, M. Kraft and R. Xu, *Nano Energy*, 2020, **77**.
35. Y. S. Jun, E. Z. Lee, X. Wang, W. H. Hong, G. D. Stucky and A. Thomas, *Advanced Functional Materials*, 2013, **23**, 3661-3667.
36. J. X. Wu, P. P. Bag, Y. T. Xu, L. Gong, C. T. He, X. M. Chen and J. P. Zhang, *Advanced Materials*, 2021, **33**, 2007368.
37. B. Li, Y. Chen, X. Ge, J. Chai, X. Zhang, T. S. A. Hor, G. Du, Z. Liu, H. Zhang and Y. Zong, *Nanoscale*, 2016, **8**, 5067-5075.
38. M. Jia, C. Choi, T.-S. Wu, C. Ma, P. Kang, H. Tao, Q. Fan, S. Hong, S. Liu, Y.-L. Soo, Y. Jung, J. Qiu and Z. Sun, *Chemical Science*, 2018, **9**, 8775-8780.
39. Q. Fan, P. Hou, C. Choi, T. S. Wu, S. Hong, F. Li, Y. L. Soo, P. Kang, Y. Jung and Z. Sun, *Advanced Energy Materials*, 2019, **10**, 1903068.
40. Q. He, Y. Zhang, H. Li, Y. Yang, S. Chen, W. Yan, J. Dong, X. M. Zhang and X. Fan, *Small*, 2022, **18**, 2108034.
41. Z. Zhang, L. Yu, Y. Tu, R. Chen, L. Wu, J. Zhu and D. Deng, *Cell Reports Physical Science*, 2020, **1**.
42. S.-Q. Liu, E. Shahini, M.-R. Gao, L. Gong, P.-F. Sui, T. Tang, H. Zeng and J.-L. Luo, *ACS Nano*, 2021, **15**, 17757-17768.
43. S. Zhou, L. J. Zhang, L. Zhu, C. H. Tung and L. Z. Wu, *Advanced Materials*, 2023, **35**, 2300923.
44. R. Lu, X. Zhang, H. Shi, Z. Zhao, M. Li and X. Zhang, *Applied Catalysis B: Environmental*, 2024, **341**, 123293.
45. D. M. Weekes, D. A. Salvatore, A. Reyes, A. Huang and C. P. Berlinguette, *Accounts of Chemical Research*, 2018, **51**, 910-918.
46. T. Wang, X. Sang, W. Zheng, B. Yang, S. Yao, C. Lei, Z. Li, Q. He, J. Lu, L. Lei, L. Dai and Y. Hou, *Advanced Materials*, 2020, **32**, 2002430.
47. S. Chen, J. Chen, Y. Li, S. Tan, X. Liao, T. Zhao, K. Zhang, E. Hu, F. Cheng and H. Wang, *Advanced Functional Materials*, 2023, **33**, 2300801.